DESY 98-029 ISSN 0418-9833

Hadron Production in Diffractive Deep-Inelastic Scattering

H1 Collaboration

Abstract

Characteristics of hadron production in diffractive deep-inelastic positron-proton scattering are studied using data collected in 1994 by the H1 experiment at HERA. The following distributions are measured in the centre-of-mass frame of the photon dissociation system: the hadronic energy flow, the Feynman-x (x_F) variable for charged particles, the squared transverse momentum of charged particles (p_T^{*2}), and the mean p_T^{*2} as a function of x_F. These distributions are compared with results in the $\gamma^* p$ centre-of-mass frame from inclusive deep-inelastic scattering in the fixed-target experiment EMC, and also with the predictions of several Monte Carlo calculations. The data are consistent with a picture in which the partonic structure of the diffractive exchange is dominated at low Q^2 by hard gluons.

Submitted to Physics Letters ***B***

C. Adloff[35], S. Aid[13], M. Anderson[23], V. Andreev[26], B. Andrieu[29], V. Arkadov[36], C. Arndt[11], I. Ayyaz[30], A. Babaev[25], J. Bähr[36], J. Bán[18], P. Baranov[26], E. Barrelet[30], R. Barschke[11], W. Bartel[11], U. Bassler[30], P. Bate[23], M. Beck[14], A. Beglarian[11], H.-J. Behrend[11], C. Beier[16], A. Belousov[26], Ch. Berger[1], G. Bernardi[30], G. Bertrand-Coremans[4], R. Beyer[11], P. Biddulph[23], J.C. Bizot[28], K. Borras[8], V. Boudry[29], A. Braemer[15], W. Braunschweig[1], V. Brisson[28], D.P. Brown[23], W. Brückner[14], P. Bruel[29], D. Bruncko[18], C. Brune[16], J. Bürger[11], F.W. Büsser[13], A. Buniatian[33], S. Burke[19], G. Buschhorn[27], D. Calvet[24], A.J. Campbell[11], T. Carli[27], E. Chabert[24], M. Charlet[11], D. Clarke[5], B. Clerbaux[4], S. Cocks[20], J.G. Contreras[8], C. Cormack[20], J.A. Coughlan[5], M.-C. Cousinou[24], B.E. Cox[23], G. Cozzika[9], J. Cvach[31], J.B. Dainton[20], W.D. Dau[17], K. Daum[40], M. David[9], A. De Roeck[11], E.A. De Wolf[4], B. Delcourt[28], C. Diaconu[24], M. Dirkmann[8], P. Dixon[21], W. Dlugosz[7], K.T. Donovan[21], J.D. Dowell[3], A. Droutskoi[25], J. Ebert[35], G. Eckerlin[11], D. Eckstein[36], V. Efremenko[25], S. Egli[38], R. Eichler[37], F. Eisele[15], E. Eisenhandler[21], E. Elsen[11], M. Enzenberger[27], M. Erdmann[15], A.B. Fahr[13], L. Favart[4], A. Fedotov[25], R. Felst[11], J. Feltesse[9], J. Ferencei[18], F. Ferrarotto[33], K. Flamm[11], M. Fleischer[8], G. Flügge[2], A. Fomenko[26], J. Formánek[32], J.M. Foster[23], G. Franke[11], E. Gabathuler[20], K. Gabathuler[34], F. Gaede[27], J. Garvey[3], J. Gayler[11], M. Gebauer[36], R. Gerhards[11], A. Glazov[36], L. Goerlich[6], N. Gogitidze[26], M. Goldberg[30], I. Gorelov[25], C. Grab[37], H. Grässler[2], T. Greenshaw[20], R.K. Griffiths[21], G. Grindhammer[27], C. Gruber[17], T. Hadig[1], D. Haidt[11], L. Hajduk[6], T. Haller[14], M. Hampel[1], V. Haustein[35], W.J. Haynes[5], B. Heinemann[11], G. Heinzelmann[13], R.C.W. Henderson[19], S. Hengstmann[38], H. Henschel[36], R. Heremans[4], I. Herynek[31], K. Hewitt[3], K.H. Hiller[36], C.D. Hilton[23], J. Hladký[31], M. Höppner[8], D. Hoffmann[11], T. Holtom[20], R. Horisberger[34], V.L. Hudgson[3], M. Hütte[8], M. Ibbotson[23], Ç. İşsever[8], H. Itterbeck[1], M. Jacquet[28], M. Jaffre[28], J. Janoth[16], D.M. Jansen[14], L. Jönsson[22], D.P. Johnson[4], H. Jung[22], M. Kander[11], D. Kant[21], U. Kathage[17], J. Katzy[11], H.H. Kaufmann[36], O. Kaufmann[15], M. Kausch[11], S. Kazarian[11], I.R. Kenyon[3], S. Kermiche[24], C. Keuker[1], C. Kiesling[27], M. Klein[36], C. Kleinwort[11], G. Knies[11], J.H. Köhne[27], H. Kolanoski[39], S.D. Kolya[23], V. Korbel[11], P. Kostka[36], S.K. Kotelnikov[26], T. Krämerkämper[8], M.W. Krasny[30], H. Krehbiel[11], D. Krücker[27], A. Küpper[35], H. Küster[22], M. Kuhlen[27], T. Kurča[36], B. Laforge[9], R. Lahmann[11], M.P.J. Landon[21], W. Lange[36], U. Langenegger[37], A. Lebedev[26], M. Lehmann[17], F. Lehner[11], V. Lemaitre[11], S. Levonian[11], M. Lindstroem[22], J. Lipinski[11], B. List[11], G. Lobo[28], V. Lubimov[25], D. Lüke[8,11], L. Lytkin[14], N. Magnussen[35], H. Mahlke-Krüger[11], E. Malinovski[26], R. Maraček[18], P. Marage[4], J. Marks[15], R. Marshall[23], G. Martin[13], R. Martin[20], H.-U. Martyn[1], J. Martyniak[6], S.J. Maxfield[20], S.J. McMahon[20], T.R. McMahon[20], A. Mehta[5], K. Meier[16], P. Merkel[11], F. Metlica[14], A. Meyer[13], A. Meyer[11], H. Meyer[35], J. Meyer[11], P.-O. Meyer[2], A. Migliori[29], S. Mikocki[6], D. Milstead[20], J. Moeck[27], R. Mohr[27], S. Mohrdieck[13], F. Moreau[29], J.V. Morris[5], E. Mroczko[6], D. Müller[38], K. Müller[11], P. Murín[18], V. Nagovizin[25], R. Nahnhauer[36], B. Naroska[13], Th. Naumann[36], I. Négri[24], P.R. Newman[3], D. Newton[19], H.K. Nguyen[30], T.C. Nicholls[11], F. Niebergall[13], C. Niebuhr[11], Ch. Niedzballa[1], H. Niggli[37], O. Nix[16], G. Nowak[6], T. Nunnemann[14], H. Oberlack[27], J.E. Olsson[11], D. Ozerov[25], P. Palmen[2], E. Panaro[11], A. Panitch[4], C. Pascaud[28], S. Passaggio[37], G.D. Patel[20], H. Pawletta[2], E. Peppel[36], E. Perez[9], J.P. Phillips[20], A. Pieuchot[11], D. Pitzl[37], R. Pöschl[8], G. Pope[7], B. Povh[14], K. Rabbertz[1], P. Reimer[31], B. Reisert[27], H. Rick[11], S. Riess[13], E. Rizvi[11], P. Robmann[38], R. Roosen[4], K. Rosenbauer[1], A. Rostovtsev[25,11], F. Rouse[7], C. Royon[9], S. Rusakov[26], K. Rybicki[6], D.P.C. Sankey[5], P. Schacht[27], J. Scheins[1], S. Schiek[11], S. Schleif[16], P. Schleper[15], W. von Schlippe[21], D. Schmidt[35], G. Schmidt[11], L. Schoeffel[9], A. Schöning[11], V. Schröder[11], H.-C. Schultz-Coulon[11], B. Schwab[15], F. Sefkow[38], A. Semenov[25], V. Shekelyan[27], I. Sheviakov[26], L.N. Shtarkov[26], G. Siegmon[17], U. Siewert[17], Y. Sirois[29], I.O. Skillicorn[10], T. Sloan[19], P. Smirnov[26], M. Smith[20], V. Solochenko[25], Y. Soloviev[26], A. Specka[29], J. Spiekermann[8], H. Spitzer[13], F. Squinabol[28], P. Steffen[11], R. Steinberg[2], J. Steinhart[13], B. Stella[33], A. Stellberger[16], J. Stiewe[16], K. Stolze[36], U. Straumann[15], W. Struczinski[2], J.P. Sutton[3], M. Swart[16], S. Tapprogge[16], M. Taševský[32],

V. Tchernyshov[25], S. Tchetchelnitski[25], J. Theissen[2], G. Thompson[21], P.D. Thompson[3], N. Tobien[11], R. Todenhagen[14], P. Truöl[38], G. Tsipolitis[37], J. Turnau[6], E. Tzamariudaki[11], S. Udluft[27], A. Usik[26], S. Valkár[32], A. Valkárová[32], C. Vallée[24], P. Van Esch[4], P. Van Mechelen[4], Y. Vazdik[26], G. Villet[9], K. Wacker[8], R. Wallny[15], T. Walter[38], B. Waugh[23], G. Weber[13], M. Weber[16], D. Wegener[8], A. Wegner[27], T. Wengler[15], M. Werner[15], L.R. West[3], S. Wiesand[35], T. Wilksen[11], S. Willard[7], M. Winde[36], G.-G. Winter[11], C. Wittek[13], E. Wittmann[14], M. Wobisch[2], H. Wollatz[11], E. Wünsch[11], J. Žáček[32], J. Zálešák[32], Z. Zhang[28], A. Zhokin[25], P. Zini[30], F. Zomer[28], J. Zsembery[9], and M. zurNedden[38]

[1] I. Physikalisches Institut der RWTH, Aachen, Germany[a]
[2] III. Physikalisches Institut der RWTH, Aachen, Germany[a]
[3] School of Physics and Space Research, University of Birmingham, Birmingham, UK[b]
[4] Inter-University Institute for High Energies ULB-VUB, Brussels; Universitaire Instelling Antwerpen, Wilrijk; Belgium[c]
[5] Rutherford Appleton Laboratory, Chilton, Didcot, UK[b]
[6] Institute for Nuclear Physics, Cracow, Poland[d]
[7] Physics Department and IIRPA, University of California, Davis, California, USA[e]
[8] Institut für Physik, Universität Dortmund, Dortmund, Germany[a]
[9] DSM/DAPNIA, CEA/Saclay, Gif-sur-Yvette, France
[10] Department of Physics and Astronomy, University of Glasgow, Glasgow, UK[b]
[11] DESY, Hamburg, Germany[a]
[12] I. Institut für Experimentalphysik, Universität Hamburg, Hamburg, Germany[a]
[13] II. Institut für Experimentalphysik, Universität Hamburg, Hamburg, Germany[a]
[14] Max-Planck-Institut für Kernphysik, Heidelberg, Germany[a]
[15] Physikalisches Institut, Universität Heidelberg, Heidelberg, Germany[a]
[16] Institut für Hochenergiephysik, Universität Heidelberg, Heidelberg, Germany[a]
[17] Institut für experimentelle und angewandte Physik, Universität Kiel, Kiel, Germany[a]
[18] Institute of Experimental Physics, Slovak Academy of Sciences, Košice, Slovak Republic[f,j]
[19] School of Physics and Chemistry, University of Lancaster, Lancaster, UK[b]
[20] Department of Physics, University of Liverpool, Liverpool, UK[b]
[21] Queen Mary and Westfield College, London, UK[b]
[22] Physics Department, University of Lund, Lund, Sweden[g]
[23] Department of Physics and Astronomy, University of Manchester, Manchester, UK[b]
[24] CPPM, Université d'Aix-Marseille II, IN2P3-CNRS, Marseille, France
[25] Institute for Theoretical and Experimental Physics, Moscow, Russia
[26] Lebedev Physical Institute, Moscow, Russia[f,k]
[27] Max-Planck-Institut für Physik, München, Germany[a]
[28] LAL, Université de Paris-Sud, IN2P3-CNRS, Orsay, France
[29] LPNHE, Ecole Polytechnique, IN2P3-CNRS, Palaiseau, France
[30] LPNHE, Universités Paris VI and VII, IN2P3-CNRS, Paris, France
[31] Institute of Physics, Academy of Sciences of the Czech Republic, Praha, Czech Republic[f,h]
[32] Nuclear Center, Charles University, Praha, Czech Republic[f,h]
[33] INFN Roma 1 and Dipartimento di Fisica, Università Roma 3, Roma, Italy
[34] Paul Scherrer Institut, Villigen, Switzerland
[35] Fachbereich Physik, Bergische Universität Gesamthochschule Wuppertal, Wuppertal, Germany[a]
[36] DESY, Institut für Hochenergiephysik, Zeuthen, Germany[a]
[37] Institut für Teilchenphysik, ETH, Zürich, Switzerland[i]
[38] Physik-Institut der Universität Zürich, Zürich, Switzerland[i]
[39] Institut für Physik, Humboldt-Universität, Berlin, Germany[a]
[40] Rechenzentrum, Bergische Universität Gesamthochschule Wuppertal, Wuppertal, Germany[a]

[a] Supported by the Bundesministerium für Bildung, Wissenschaft, Forschung und Technologie, FRG, under contract numbers 7AC17P, 7AC47P, 7DO55P, 7HH17I, 7HH27P, 7HD17P, 7HD27P, 7KI17I, 6MP17I and 7WT87P
[b] Supported by the UK Particle Physics and Astronomy Research Council, and formerly by the UK Science and Engineering Research Council
[c] Supported by FNRS-NFWO, IISN-IIKW
[d] Partially supported by the Polish State Committee for Scientific Research, grant no. 115/E-343/SPUB/P03/002/97 and grant no. 2P03B 055 13
[e] Supported in part by US DOE grant DE F603 91ER40674
[f] Supported by the Deutsche Forschungsgemeinschaft
[g] Supported by the Swedish Natural Science Research Council
[h] Supported by GA ČR grant no. 202/96/0214, GA AV ČR grant no. A1010619 and GA UK grant no. 177
[i] Supported by the Swiss National Science Foundation
[j] Supported by VEGA SR grant no. 2/1325/96
[k] Supported by Russian Foundation for Basic Researches grant no. 96-02-00019

1 Introduction

Studies of the 1992 deep-inelastic electron-proton scattering events (DIS) at HERA [1] revealed the presence of "rapidity-gap events" – events of the form $ep \to eXY$ in which the hadronic final state consists of two parts, X and Y, separated by a large region in pseudorapidity in which no hadrons are observed. This is illustrated in figure 1. The masses M_X and M_Y of these two systems, separated by the largest rapidity gap in the event, are thus small compared to W, the invariant mass of the $\gamma^* p$ system. The system Y in these events consists of a proton or other low-mass hadronic state and has a momentum similar to that of the incoming proton. The magnitude of the square of the 4-momentum transferred to X from the proton, $|t|$, is small ($\lesssim 1\,\mathrm{GeV}^2$). The contribution of these events to the ep interaction cross section has been measured in terms of a diffractive structure function, $F_2^{D(3)}$, using the HERA data of 1993 [2]. The more precise $F_2^{D(3)}$ measurements made with the 1994 data [3] indicate that the cross section for rapidity-gap events may be parameterised as a diffractive contribution, from pomeron ($I\!P$) exchange, together with a contribution from meson exchange. The pomeron contribution dominates for small values ($\lesssim 0.05$) of the variable $x_{I\!P}$, which is the fraction of the incoming proton's longitudinal momentum carried by the exchange. Furthermore, the pomeron may be interpreted as having partonic structure.

A QCD study of parton distribution functions [3], evolved according to the DGLAP equations [4], reveals the preference of the $F_2^{D(3)}$ data for a pomeron that is dominated by a "hard-gluon" parton distribution at the starting scale of $Q_0^2 = 3\,\mathrm{GeV}^2$ (fits 2 and 3 in [3]), i.e. a distribution with a large contribution from gluons carrying a significant fraction of the momentum of the pomeron. A pomeron model with only quarks at Q_0^2 (fit 1 in [3]) fails.

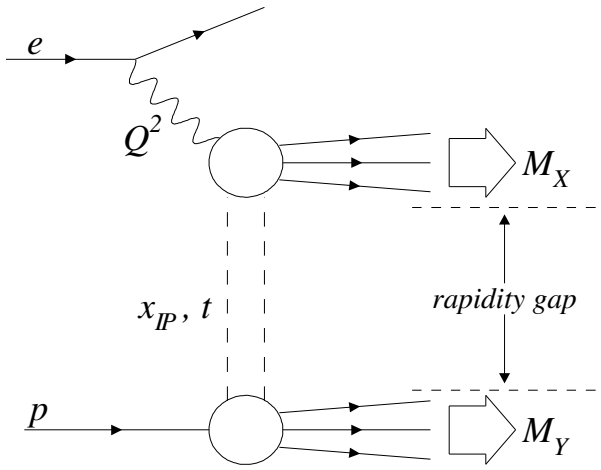

Figure 1: Schematic picture of a deep-inelastic interaction $ep \to eXY$ with a "rapidity gap" devoid of hadronic energy. The high-Q^2 virtual photon interacts with a colourless space-like entity of squared 4-momentum t, whose longitudinal momentum as a fraction of that of the target proton is $x_{I\!P}$; the direction of the system Y is close to that of the target proton.

The studies of the diffractive final state presented here may be regarded as specific tests of the pomeron structure extracted from $F_2^{D(3)}$, complementary to other final-state analyses [5, 6, 7]. A gluon-dominated pomeron is expected to interact largely by boson-gluon fusion (BGF); the transverse momenta of the outgoing partons relative to the photon direction in the $\gamma^* I\!P$ centre-of-mass (CM) frame (i.e. the CM frame of the photon dissociation system X), as well as the amount of gluon radiation and consequently the parton multiplicity, are therefore likely to be greater than in the case of a quark-dominated pomeron.

The partonic structure of the pomeron should thus be reflected in the energy-flow and charged-particle distributions in the $\gamma^* I\!P$ CM frame. These distributions are compared here with data on deep-inelastic μp interactions in the $\gamma^* p$ CM frame at the EMC experiment. This provides a comparison of the structure of the pomeron with that of the proton.

The distributions are also compared with predictions from a calculation using a pomeron with parton distributions from the best QCD fit to $F_2^{D(3)}$ (fit 3). Comparison with predictions from a calculation with only quarks in the pomeron at the starting scale of the QCD fit (fit 1) demonstrates the sensitivity of the measurements to the parton distributions of the pomeron.

Another approach to diffractive DIS is provided by the photon dissociation picture [8]. In the rest frame of the proton, the photon fluctuates a long time before the interaction into a Fock state with definite parton content ($q\bar{q}$, $q\bar{q}g$, ...), and this partonic state scatters diffractively off the proton. Scattering from a quark in the pomeron corresponds to an Aligned Jet Model [9] topology in this picture, whereas scattering from a gluon corresponds to Fock states with one or more gluons and results in less pronounced alignment.

A non-diffractive model for the production of events with a large rapidity gap has also been proposed, using a conventional picture of DIS based on scattering from a single parton within the proton, followed by soft colour interactions [10, 11]. The data are also compared with predictions of this model.

2 Detector, Event Selection and Kinematics

The data used here were collected in 1994 with the H1 detector at the HERA collider, which operated with 27.5 GeV positron and 820 GeV proton beams. The H1 detector is described in detail elsewhere [12]; those components of importance for the analyses presented here are briefly mentioned in the following. The laboratory coordinate system has its origin at the nominal interaction point and its z axis in the proton beam direction, also called the forward direction. The pseudorapidity is defined as $\eta = -\ln\tan\frac{\theta}{2}$, where θ is the angle with respect to the z axis.

In the forward and central regions the interaction point is surrounded by a system of tracking detectors – interleaved drift and multi-wire proportional chambers – which cover the pseudorapidity range $-1.5 < \eta < 2.8$ and the full azimuth. The momenta of charged particles are determined for this analysis from their track curvature in the central jet chamber (CJC) in the uniform magnetic field of strength 1.15 T generated by a superconducting solenoid. The CJC has a resolution of $\sigma_{p_T}/p_T \approx 0.006 p_T \oplus 0.008$ (where p_T is in GeV and the constant term describes the contribution from multiple scattering at $p_T = 0.5$ GeV) and $\sigma_\theta \approx 20$ mrad. The solenoid surrounds the trackers and the fine-grained liquid-argon (LAr) calorimeter, which covers the range $-1.5 < \eta < 3.6$ and is used to measure energies in the hadronic final state with a resolution of $\sigma_E/E \approx 0.5/\sqrt{E} \oplus 0.02$ (where E is in GeV) [12]. Charged-particle detection in the backward region, $-3.1 < \eta < -1.5$, is provided by the backward proportional chamber (BPC). Behind this, the backward electromagnetic calorimeter (BEMC) completes the calorimetric coverage in the range $-3.5 < \eta < -1.5$.

Several subdetectors in the forward region are used in this analysis to tag particles emitted close to the proton direction. These detectors cover a range larger than their purely geometrical acceptance, due to the effect of secondaries resulting from the scattering of primary particles in the beam pipe and adjacent material. The copper-silicon plug calorimeter covers the range $3.5 < \eta < 5.5$. The first three double layers of drift chambers in the forward muon detector (FMD) are sensitive to particles in the range $5.0 < \eta < 6.5$. The proton-remnant tagger (PRT), comprising a set of double layers of scintillators situated around the proton beam pipe, covers the range $6.0 < \eta < 7.5$.

The luminosity is determined from the rate of Bethe-Heitler interactions detected in a monitor downstream of the main detector in the positron direction. The total luminosity analysed here amounts to approximately $2\,\mathrm{pb}^{-1}$.

All events included in this analysis are required to have a scattered positron reconstructed with an energy greater than 12 GeV, emitted in the angular range $156^\circ < \theta < 173^\circ$. The scattered positron is identified by looking for the highest-energy cluster in the BEMC. This cluster is required to be associated with a hit in the BPC and to pass a cut on its transverse size. The trigger used to select these events for read-out requires the presence of an energy deposit of at least 4 GeV in the BEMC. The efficiency of the BEMC trigger for positron energies larger than 10 GeV is known to exceed 99% [13]. For events passing the above selection the photoproduction background is less than 1%.

The data are selected to lie in the kinematic region $7.5 < Q^2 < 100\,\mathrm{GeV}^2$ and $0.05 < y < 0.6$. These variables are defined as $Q^2 = -q^2$ and $y = (q \cdot p)/(k \cdot p) \simeq (W^2 + Q^2)/s$, where p, k and q are the 4-momenta of the incoming proton, positron and photon respectively, W is the CM energy of the $\gamma^* p$ system, and s is the squared CM energy of the ep system. The variables Q^2 and y are calculated from the measured energy and angle of the scattered positron.

Diffractive events are recognised by the rapidity gap between the outgoing hadronic systems X and Y. This gap is tagged by the absence of signals above noise in the forward components of the H1 detector [3, 14]: the plug calorimeter, the FMD and the PRT. There must also be no energy deposit of more than 400 MeV in the forward region ($\eta > 3.0$) of the LAr calorimeter.

The variable $x_{I\!P}$ is defined as

$$x_{I\!P} = \frac{q \cdot I\!P}{q \cdot p}$$

where $I\!P$ is the 4-momentum exchanged between systems X and Y, and is reconstructed using the relation

$$x_{I\!P} \simeq \frac{1}{2E_p} \sum_{e+X} (E + p_z).$$

Here, E_p is the energy of the incoming proton, E and p_z are the energy and longitudinal momentum of each final-state particle in the laboratory frame, and the sum runs over the scattered positron e and all detected particles in the photon dissociation system X. The particles are reconstructed using a combination of tracks and calorimeter clusters, with an algorithm for track-cluster association avoiding double counting [15]. In order to enhance the contribution from pomeron exchange and to reduce the contribution from meson exchange, the requirement $x_{I\!P} < 0.025$ is made. The fraction of the exchanged momentum $I\!P$ carried by the struck quark is given by β, where

$$\beta = \frac{Q^2}{2q \cdot I\!P} \simeq \frac{Q^2}{Q^2 + M_X^2}.$$

Neither the squared momentum transfer t nor the mass M_Y of the hadronic system Y is measured here. However, the requirement of the absence of activity in the forward detectors imposes the approximate restrictions $M_Y < 1.6\,\mathrm{GeV}$ and $|t| < 1\,\mathrm{GeV}^2$, and the results are corrected to this kinematic region. Since M_Y is not measured, it is not possible to distinguish events containing an elastically scattered proton from those in which the proton dissociates into a low-mass state.

The analyses are performed in the $\gamma^* I\!P$ CM frame, the 4-momentum of the $\gamma^* I\!P$ system being reconstructed as $V = q + x_{I\!P} p$ [16]. The transverse momentum of the pomeron with respect to the direction of the incoming proton is not measured, but can be neglected since this has no significant effect on the measurements presented here.

The energy-flow distribution is measured using energy deposits reconstructed from clusters of cells in the LAr and BEMC. The clusters are required to have an energy in the range $0 < E < 25\,\mathrm{GeV}$ and to lie in the angular range $-3 < \eta < 4$. The charged-particle distributions are measured using only particles that are detected in the CJC, originate from the ep interaction vertex in the angular region $-1.31 < \eta < 1.31$, and have a transverse momentum in the laboratory frame of $0.15 < p_T < 10\,\mathrm{GeV}$, but the results are fully corrected with Monte Carlo simulations (see below) to cover the whole hadronic system.

Two variables are calculated for each charged particle, both defined in the CM frame of the $\gamma^* I\!P$ system. The Feynman-x variable, x_F, is defined as

$$x_F = \frac{2p^*_{\parallel}}{M_X},$$

where $p^*_{\parallel}$ is the component of the particle's momentum in the direction of motion of the incoming photon. In non-diffractive DIS, x_F is defined in the $\gamma^* p$ CM frame, and the denominator is W. Positive x_F corresponds to the current hemisphere and negative x_F to the target fragmentation hemisphere. The other variable used here, p^*_T, is the transverse momentum of the particle with respect to the photon direction.

3 Monte Carlo Models for Diffractive Interactions

Monte Carlo calculations employing the event generator RAPGAP 2.02 [17] are used in conjunction with a detailed simulation of the H1 apparatus to correct the experimental distributions for the acceptance and resolution of the detector, and later to compare the results with theoretical expectations. The data are also compared with the predictions of the Monte Carlo generator LEPTO 6.5 [11].

The RAPGAP model treats diffractive interactions as inelastic $eI\!P$ collisions, the pomeron being modelled as an object with partonic substructure. Scattering on mesons is also included.

For scattering from quarks, the lowest-order diagram considered by RAPGAP at the parton level is $\mathcal{O}(\alpha)$ $eq \to eq$ scattering (figure 2a); a higher-order, $\mathcal{O}(\alpha\alpha_s)$, process is QCD Compton (QCD-C) scattering $eq \to eqg$ (figure 2b). For scattering from gluons, the lowest-order $\mathcal{O}(\alpha\alpha_s)$ process is boson-gluon fusion $eg \to eq\bar{q}$ (figure 2c). A cut $\hat{p}_T^2 > 2\,\mathrm{GeV}^2$ is applied in order to avoid divergences in the $\mathcal{O}(\alpha\alpha_s)$ matrix elements for massless quarks, $\hat{p}_T$ being the transverse momentum of the outgoing partons with respect to the photon direction in the CM frame of the hard subprocess. For $\hat{p}_T^2 < 2\,\mathrm{GeV}^2$, only $eq \to eq$ scattering is used. In the RAPGAP model, a "pomeron remnant" is implicit at the parton level, consisting of a quark (antiquark) in eq ($e\bar{q}$) scattering and a gluon in the eg case (see figure 2). The renormalisation and factorisation scale μ^2 is set to Q^2. Higher-order corrections at the parton level are treated using leading-log parton showers (PS) [18] as implemented in RAPGAP. Subsequent hadronisation is simulated according to the Lund string model in JETSET [19]. The dependence of the acceptance corrections on the method used to handle higher-order corrections in RAPGAP is studied with a separate calculation in which QCD-C and higher-order processes are simulated by the colour-dipole (CD) model [20]. RAPGAP is interfaced to HERACLES [21] for the simulation of QED radiative effects.

For the comparisons presented here, two sets of parton distributions for the pomeron are used in the RAPGAP generator. The first is taken from the best fit to the Q^2 and β dependence of the diffractive structure function $F_2^{D(3)}$ (fit 3 in [3]). It is characterised by a hard gluon distribution at the starting scale for DGLAP evolution, $Q_0^2 = 3\,\mathrm{GeV}^2$, in which gluons carry $\gtrsim 80\%$ of the

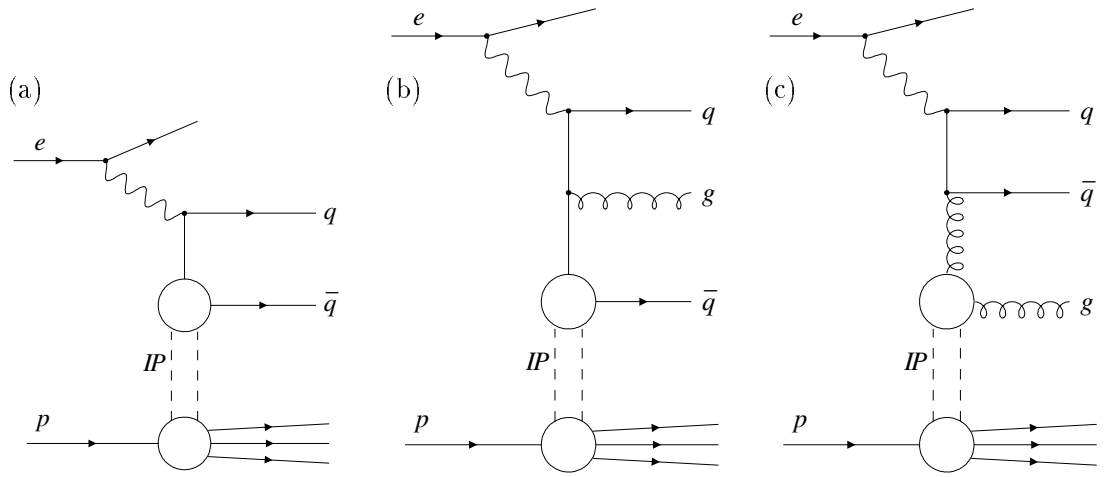

Figure 2: Elementary processes included in the RAPGAP simulation of ep diffractive interactions: (a) lowest-order, $\mathcal{O}(\alpha)$, e scattering from a quark, leading to a two-parton configuration; (b) one of the diagrams for the QCD-C process, $\mathcal{O}(\alpha\alpha_s)$; (c) lowest-order, $\mathcal{O}(\alpha\alpha_s)$, e scattering from a gluon by BGF, leading to a three-parton configuration.

total momentum of the diffractive exchange[1]. The second is taken from a fit in which only quarks are permitted to contribute to the partonic structure of the pomeron at $Q^2 = Q_0^2$ (fit 1 in [3]). The latter choice does not provide a satisfactory description of the $F_2^{D(3)}$ measurements; it is used here to demonstrate the sensitivity of the results to the parton distributions of the pomeron. The predictions of RAPGAP with these two sets of parton distributions are hereafter referred to as RG–F_2^D (fit 3) and RG–F_2^D (fit 1) respectively. The meson structure function is taken to be that of the pion [22]. In both cases, the parton distribution functions evolve with Q^2 according to the DGLAP equations. The partons are treated as having no intrinsic k_T.

In the LEPTO 6.5 model, rapidity-gap events are generated by the soft colour interaction (SCI) mechanism. Deep-inelastic scattering is modelled using the matrix elements for processes up to $\mathcal{O}(\alpha\alpha_s)$, as in RAPGAP, but with partons coming directly from the proton according to the MRS(H) parameterisation [23] of the proton structure function, in which the renormalisation and factorisation scale μ^2 is again set to Q^2. The divergences in the $\mathcal{O}(\alpha\alpha_s)$ matrix elements are avoided using the cuts $\hat{s} > \hat{s}_{min}$ and $z_q < z_{q,min} < 1 - z_q$, where $\hat{s}$ is the CM energy of the hard subprocess, $z_q = (p \cdot p_q)/(p \cdot q)$ and p_q is the 4-momentum of one of the outgoing partons. The parameters $\hat{s}_{min}$ and $z_{q,min}$ are set to $4\,\mathrm{GeV}^2$ and 0.04 respectively. Higher-order corrections are treated with the PS method, and hadronisation follows the Lund string model. Further non-perturbative interactions take place as the outgoing partons pass through the colour field of the proton. These soft colour interactions can result in a hadronic final state comprising two colour-singlet systems separated by a rapidity gap.

4 Acceptance Corrections and Systematic Errors

The data are corrected for the acceptance and resolution of the H1 apparatus using events generated by RAPGAP 2.02 [17] with a hard-gluon pomeron structure function. The following sources of systematic error are taken into account; the errors shown in brackets are those on the energy flow and the charged particle distributions respectively:

[1]Fits 2 and 3 in [3] give very similar predictions for the distributions studied here. Only the predictions from fit 3 are shown in this paper.

- an uncertainty in the LAr calibration for hadronic energy of $\pm 4\%$, leading to an average error in the experimental distributions of $\pm(6\%, 2\%)$;
- an uncertainty in the BEMC calibration for hadronic energy of $\pm 20\%$, leading to an average error of $\pm(6\%, 0.7\%)$;
- an uncertainty of $\pm 1\%$ in the positron energy scale, leading to an average error of $\pm(3\%, 0.5\%)$;
- an uncertainty of ± 1 mrad in the positron polar angle, leading to an average error of $\pm(0.5\%, 0.5\%)$;
- an uncertainty in the $x_{I\!P}$ dependence in the Monte Carlo used to calculate the acceptance corrections, taken into account by reweighting the generated events with the function $x_{I\!P}^{\pm 0.2}$, resulting in an average error of $\pm(8\%, 3\%)$;
- an uncertainty in the β dependence in the Monte Carlo, taken into account by reweighting the generated events with the function $(a^{-1} - a)\beta + a$, where a has the range 0.5 to 2, resulting in an average error of $\pm(6\%, 1\%)$;
- an uncertainty in the t dependence in the Monte Carlo, taken into account by reweighting the generated events with the function $e^{\pm 2t}$, resulting in an average error of $\pm(5\%, 2\%)$;
- uncertainties arising from the method used to treat higher-order corrections in the Monte Carlo; this results in an error of $\pm(10\%, 10\%)$, evaluated by taking the full difference between the results obtained using the PS and CD models as an estimation of the extrapolation uncertainty from the Monte Carlo.

In the charged-particle analysis, the track selection criteria were varied to allow for the imperfect description of the Central Tracker in the Monte Carlo. The selection was varied by increasing the angular range of the tracks to $-1.50 < \eta < 1.64$ and by requiring the radial track length to be greater than 15 cm and the number of hits on a track N_{hits} to be greater than 10. This results in an average error of $\pm 5\%$, rising in the low-x_F region to 20% in the x_F distribution and 15% in $\langle p_T^{*2} \rangle$ in the "seagull plot" (figure 6).

5 Results

Results[2] are shown for the kinematic range $7.5 < Q^2 < 100\,\mathrm{GeV}^2$, $0.05 < y < 0.6$, $x_{I\!P} < 0.025$, $|t| < 1\,\mathrm{GeV}^2$ and $M_Y < 1.6\,\mathrm{GeV}$. All distributions are fully corrected for the effects of the acceptance and resolution of the H1 apparatus, and statistical and systematic errors on the data points are combined quadratically. The inner vertical error bars indicate the statistical error and the outer bars the total error. Due to the $x_{I\!P}$ cut, the meson-exchange contribution is small ($< 7\%$ in the RG–F_2^D (fit 3) model) and does not affect the conclusions.

It is shown below that, in Monte Carlo calculations, the characteristic features of the parton content of the pomeron are reflected in the distributions of various final-state observables. The data are therefore compared with data on $\gamma^* p$ interactions at relatively high Bjorken-x values ($x > 0.01$), where the structure of the proton is dominated by quarks. The data used for this comparison are taken from μp interactions at the EMC experiment [24], with the mean $\gamma^* p$ CM energy, $\langle W \rangle = 14\,\mathrm{GeV}$, of the EMC inclusive DIS data similar to the mean $\gamma^* I\!P$ CM energy, $\langle M_X \rangle \approx 12\,\mathrm{GeV}$, of the H1 diffractive data.

[2]The data are available in numerical form on request and have also been submitted to the Durham HEPDATA database `http://durpdg.dur.ac.uk/HEPDATA`.

The experimental data are also compared with the predictions of the RAPGAP model with the two different pomeron structures from the DGLAP fits to $F_2^{D(3)}$ – the preferred hard-gluon structure (RG–F_2^D (fit 3)) and the structure with only quarks at the starting scale (RG–F_2^D (fit 1)) – as well as with the soft colour interaction (SCI) model as implemented in LEPTO 6.5.

In the CM frame of the $\gamma^* I\!P$ system, a model with a quark-dominated pomeron results in events in which the struck quark and the pomeron remnant tend to be close to the $\gamma^* I\!P$ axis. Large contributions to the transverse momentum can arise from QCD corrections such as QCD Compton scattering, but the rate of these is suppressed by a factor α_s. In contrast, if the pomeron is a gluon-dominated object, more transverse momentum and energy flow are produced at lowest order. This arises because the quark propagator in the BGF process can have non-zero virtuality, so the quark-antiquark pair from the hard subprocess is not necessarily aligned along the $\gamma^* I\!P$ axis. Evidence for this effect is seen in a recent analysis, using the same data, of the distribution of the p_T of thrust jets relative to the $\gamma^* I\!P$ axis [6]. In both the quark- and gluon-dominated cases, small contributions to the transverse momentum are generated by the intrinsic k_T of the partons, by the hadronisation process, and by particle decays. However, it is known from the average thrust distribution shown in [6] that a quark-dominated exchange, even with large intrinsic k_T, would not be able to explain the relatively low value of the average thrust.

Figure 3 shows the event-normalised energy flow $1/N\ \mathrm{d}E/\mathrm{d}\eta^*$ in three different regions of M_X, η^* being the pseudorapidity relative to the direction of motion of the incoming photon in the CM frame of the $\gamma^* I\!P$ system and N being the number of events. The distribution is approximately symmetrical about $\eta^* = 0$, with similar levels of energy flow in the two hemispheres. At higher masses, $M_X > 8\,\mathrm{GeV}$, a two-peaked structure is seen, indicating that the major topological property of these events is of a 2-jet nature (current jet and remnant jet).

The data are well described by the RG–F_2^D (fit 3) model[3], and for $M_X > 8\,\mathrm{GeV}$ by LEPTO 6.5, whereas the RG–F_2^D (fit 1) model predicts too much energy flow at the largest accessible pseudorapidity and fails to account for the observed energy flow in the central region, $\eta^* \approx 0$.

These features can be related to the gluon content of the pomeron and to the role of BGF. The transverse momentum generated by this process reduces the accessible pseudorapidity range along the $\gamma^* I\!P$ axis at fixed M_X and induces additional energy flow in more central regions. In addition, more energy is expected in the central region for a gluon-dominated than for a quark-dominated object because of the exchange of a gluon in BGF; this results in a colour octet-octet field between the outgoing quarks and the gluonic remnant (which all together form an overall colour singlet), giving rise to enhanced soft gluon radiation compared to the triplet-antitriplet field between the struck quark and the remnant in eq scattering [16, 25]. This effect has been seen for gluon jets produced in e^+e^- interactions [26]. This enhancement is also apparent in the virtual photon dissociation picture [8], where the process corresponding to BGF involves a Fock state containing a low-energy gluon.

The production of charged particles is studied using the distributions of the variables x_F and p_T^{*2}, defined in section 2. The results are shown for the restricted mass range $8 < M_X < 18\,\mathrm{GeV}$ in order to make the data more directly comparable with the EMC $\gamma^* p$ results.

The x_F distribution, normalised by the number of events N, is shown in figure 4. A feature of the diffractive data is the similarity between the x_F distributions in the two hemispheres, in contrast to the strong asymmetry of the $\gamma^* p$ data. The asymmetry in the latter case is explained

[3]The $\hat{p}_T^2$ cut in the generator was varied from 2 up to $4\,\mathrm{GeV}^2$ without affecting the conclusions drawn from the distributions presented in this paper.

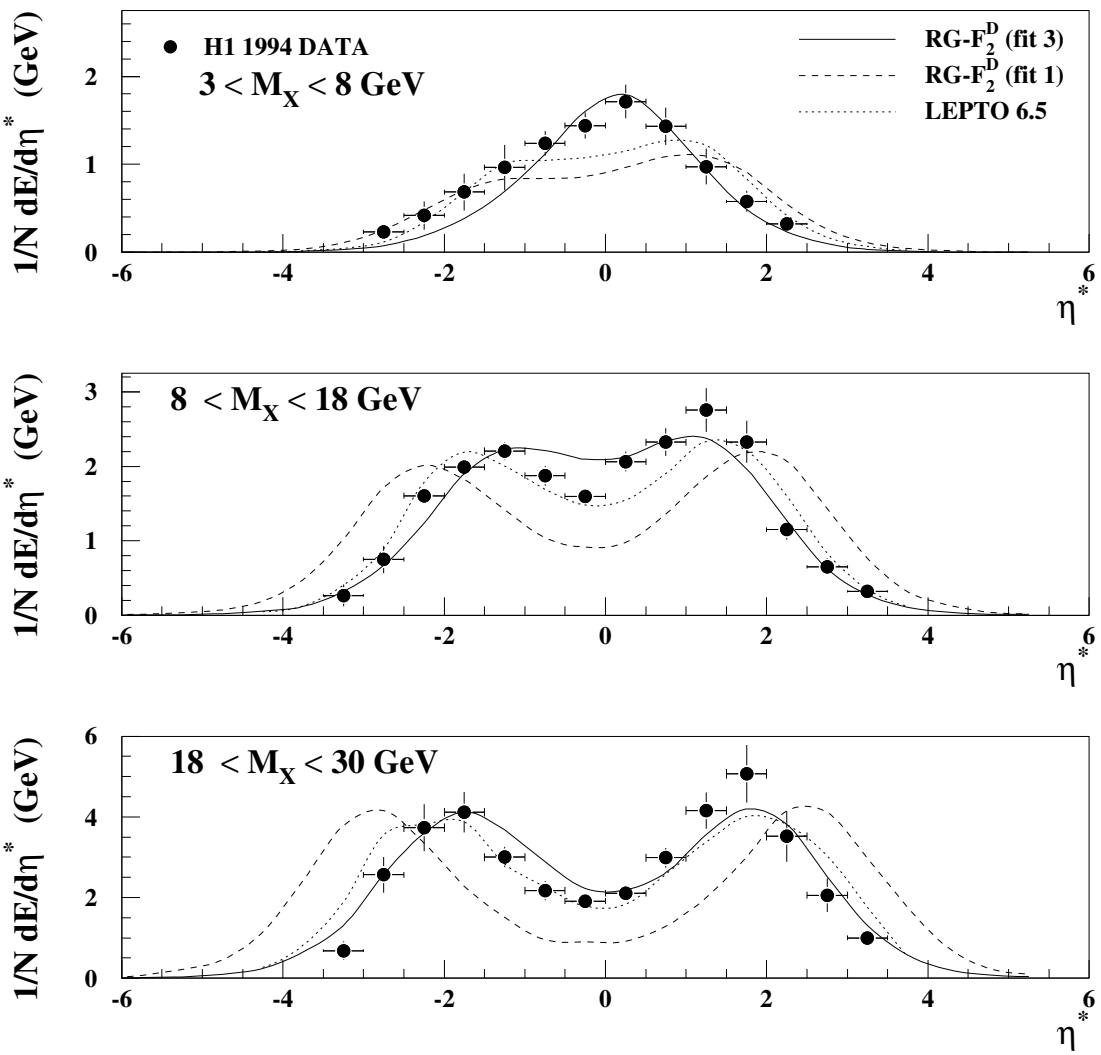

Figure 3: The energy-flow distribution in the $\gamma^* I\!P$ CM frame for three different M_X intervals, in the kinematic region $7.5 < Q^2 < 100\,\mathrm{GeV}^2$, $0.05 < y < 0.6$, $x_{I\!P} < 0.025$, $|t| < 1\,\mathrm{GeV}^2$ and $M_Y < 1.6\,\mathrm{GeV}$. Positive η^* corresponds to the direction of motion of the incoming photon. The statistical error bars are hidden by the symbols. The points are plotted at the centre of the bin in the horizontal coordinate, and the horizontal bars indicate the width of the bin. Also shown are the predictions of the following Monte Carlo models: RAPGAP with the hard-gluon pomeron structure taken from fit 3 in [3] (RG–$\mathrm{F}_2^{\mathrm{D}}$ (fit 3)); RAPGAP with the pomeron structure containing only quarks at the starting scale, taken from fit 1 in [3] (RG–$\mathrm{F}_2^{\mathrm{D}}$ (fit 1)); and the soft colour interaction model as implemented in LEPTO 6.5. The particles are taken as massless for this distribution.

by the requirement of baryon number conservation in ep interactions. This results in a large contribution from baryons in the region $x_F \lesssim -0.4$ [24].

The x_F distribution is well described by the RG–$\mathrm{F}_2^{\mathrm{D}}$ (fit 3) and LEPTO 6.5 models, whereas the RG–$\mathrm{F}_2^{\mathrm{D}}$ (fit 1) calculation fails in that it predicts too little particle production in the central region ($x_F \approx 0$) and too much particle production at large $|x_F|$. These features are related to those observed in the energy-flow distribution: longitudinal phase space is restricted because of the transverse momentum generated by the BGF process, and there is additional radiation in the central region for a gluon-dominated object.

The p_T^{*2} distribution, normalised by the number of events N, is shown in figure 5. Results

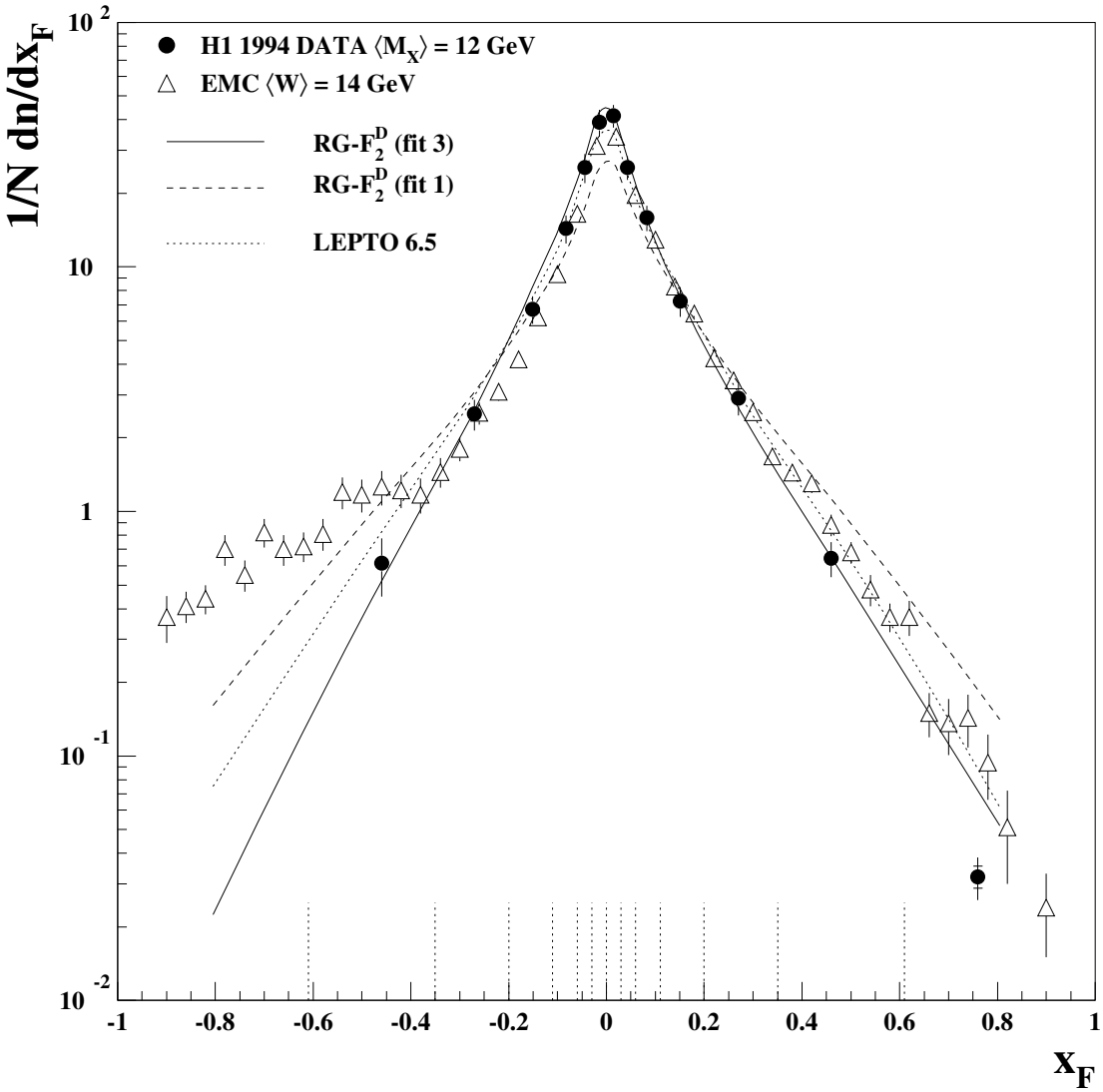

Figure 4: The Feynman-x (x_F) distribution, showing H1 $\gamma^*I\!P$ data in the $\gamma^*I\!P$ CM frame in the kinematic region $7.5 < Q^2 < 100\,\mathrm{GeV}^2$, $0.05 < y < 0.6$, $x_{I\!P} < 0.025$, $8 < M_X < 18\,\mathrm{GeV}$, $|t| < 1\,\mathrm{GeV}^2$ and $M_Y < 1.6\,\mathrm{GeV}$, together with EMC μp DIS data in the $\gamma^* p$ CM frame. Positive x_F corresponds to the direction of motion of the incoming photon. Each point is plotted at the horizontal position where the predicted probability density function has its mean value in the bin, as prescribed in [27]. The uncertainty in the horizontal position due to the model-dependence of the shape of the distribution is indicated by horizontal bars, but in most cases is contained within the width of the symbol. The bin boundaries are marked by vertical dotted lines. Also shown are the predictions of the following Monte Carlo models for the H1 data: RAPGAP with the hard-gluon pomeron structure taken from fit 3 in [3] (RG–$\mathrm{F}_2^{\mathrm{D}}$ (fit 3)); RAPGAP with the pomeron structure containing only quarks at the starting scale, taken from fit 1 in [3] (RG–$\mathrm{F}_2^{\mathrm{D}}$ (fit 1)); and the soft colour interaction model as implemented in LEPTO 6.5.

are shown for the range $0.2 < x_F < 0.4$. This restricts the data to the current region, where a comparison between H1 and EMC data is more meaningful, and matches the x_F range chosen by EMC. The number of high-p_T^* charged particles ($p_T^{*2} \gtrsim 2.0\ \mathrm{GeV}^2$) is significantly higher in the $\gamma^*I\!P$ data than in the EMC $\gamma^* p$ data. This points to a larger contribution from scattering from gluons in the diffractive case than in inclusive DIS.

The p_T^{*2} distribution is well described by the RG–$\mathrm{F}_2^{\mathrm{D}}$ (fit 3) calculation, which predicts a harder spectrum than the RG–$\mathrm{F}_2^{\mathrm{D}}$ (fit 1) model because of the role of the BGF process. The data are also well described by LEPTO 6.5. The RG–$\mathrm{F}_2^{\mathrm{D}}$ (fit 1) model does not describe the

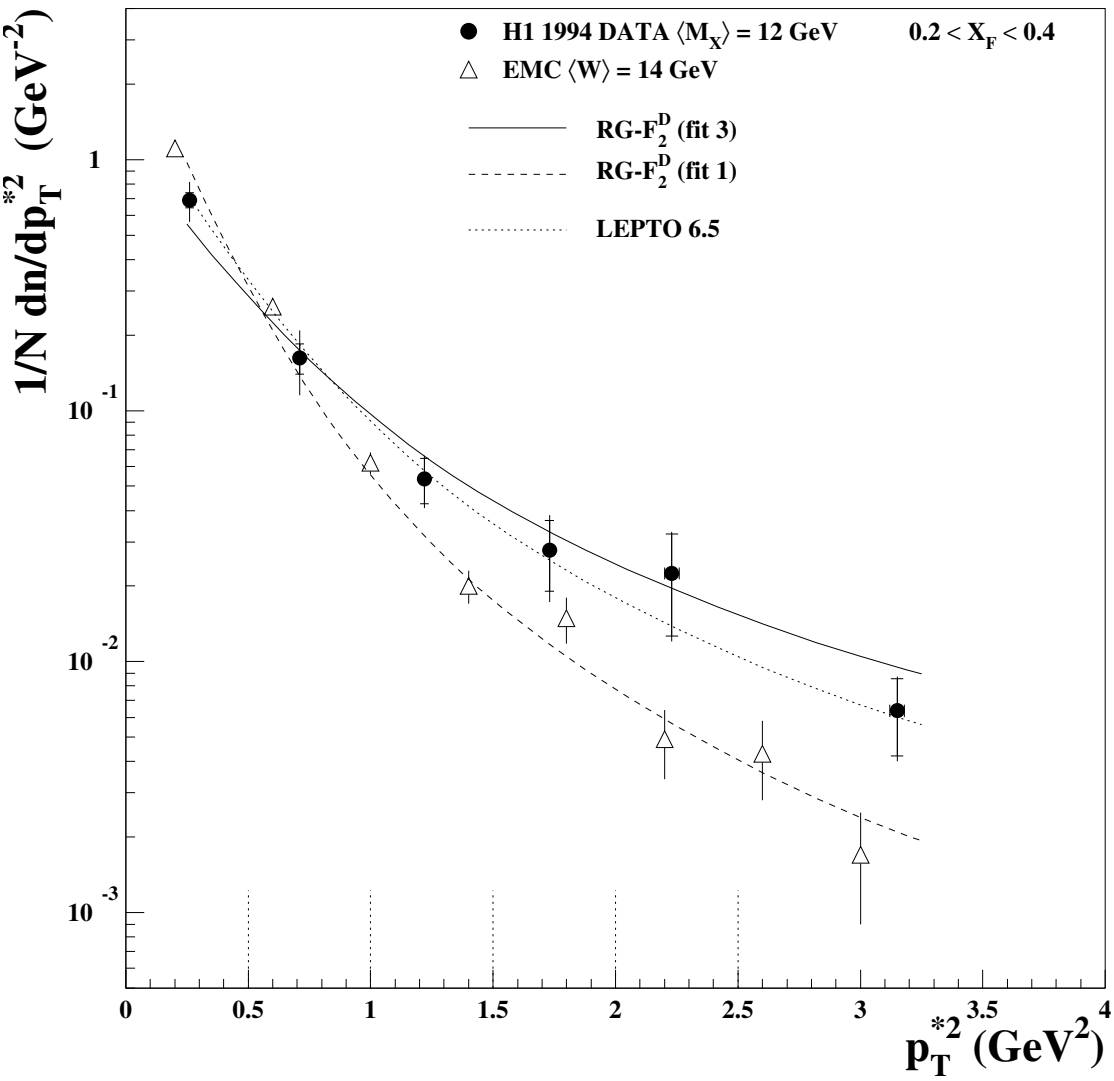

Figure 5: The p_T^{*2} distribution, showing H1 $\gamma^* I\!P$ data in the $\gamma^* I\!P$ CM frame in the kinematic region $7.5 < Q^2 < 100\,\mathrm{GeV}^2$, $0.05 < y < 0.6$, $x_{I\!P} < 0.025$, $8 < M_X < 18\,\mathrm{GeV}$, $|t| < 1\,\mathrm{GeV}^2$, $M_Y < 1.6\,\mathrm{GeV}$, and $0.2 < x_F < 0.4$, together with EMC μp DIS data in the $\gamma^* p$ CM frame. Each point is plotted at the horizontal position where the predicted probability density function has its mean value in the bin, as prescribed in [27]. The uncertainty in the horizontal position due to the model-dependence of the shape of the distribution is indicated by horizontal bars, but in most cases is contained within the width of the symbol. The bin boundaries are marked by vertical dotted lines. Also shown are the predictions of the following Monte Carlo models for the H1 data: RAPGAP with the hard-gluon pomeron structure taken from fit 3 in [3] (RG–$\mathrm{F}_2^{\mathrm{D}}$ (fit 3)); RAPGAP with the pomeron structure containing only quarks at the starting scale, taken from fit 1 in [3] (RG–$\mathrm{F}_2^{\mathrm{D}}$ (fit 1)); and the soft colour interaction model as implemented in LEPTO 6.5.

distribution well at high p_T^{*2}. It should also be noted that the RG–$\mathrm{F}_2^{\mathrm{D}}$ (fit 1) predictions for the p_T^{*2} distribution are in good agreement with the EMC $\gamma^* p$ data. This supports the argument that the EMC data (at a mean Q^2 of $12\,\mathrm{GeV}^2$) are dominated by quarks and that the higher p_T^{*2} in the diffractive data is not an effect of the larger Q^2 at H1 (where the mean Q^2 in this analysis is $25\,\mathrm{GeV}^2$).

Confirmation of the general trends discussed above is obtained from the "seagull plot", shown in figure 6, in which the mean transverse momentum squared, $\langle p_T^{*2} \rangle$, is plotted as a function of x_F. It is observed that $\langle p_T^{*2} \rangle$ is significantly higher in the H1 diffractive data than in the EMC

$\gamma^* p$ data at all but the highest x_F values, confirming the conclusions drawn from the comparisons in figure 5. The seagull plot also shows a greater degree of symmetry than is present in the $\gamma^* p$ data (cf. figure 4). As well as the effect of baryon number conservation, this is indicative of more parton radiation in the target fragmentation region. This is consistent with having a more point-like partonic system in the target fragmentation hemisphere in the diffractive data than in the $\gamma^* p$ data, where the extended nature of the proton remnant leads to a restricted phase space for parton radiation. Note, however, that there might be an indication of a small asymmetry between the two hemispheres in the energy-flow distribution (figure 3).

The significant increase in $\langle p_T^{*2} \rangle$ as $|x_F|$ increases from 0 to ~ 0.5 is well described by the RG–$\mathrm{F_2^D}$ (fit 3) calculation and reasonably well described by LEPTO 6.5, whereas the $\langle p_T^{*2} \rangle$ values predicted by the RG–$\mathrm{F_2^D}$ (fit 1) model are too low across most of the x_F range, in accordance with the above discussion of figure 5.

6 Summary and Conclusions

Energy-flow and charged-particle spectra have been measured in diffractive deep-inelastic scattering at HERA in the centre-of-mass (CM) frame of the photon dissociation ($\gamma^* I\!P$) system. The data support the conclusion reached in the analysis of the diffractive structure function $F_2^{D(3)}$ that, at low Q^2, the momentum of the diffractive exchange is carried largely by hard gluons. Thus, significant transverse momentum and energy flow are produced by the hard subprocess in the boson-gluon fusion mechanism, and also arise from the enhanced soft gluon radiation associated with the gluon from the diffractive exchange. In the photon dissociation picture, the same data can correspondingly be interpreted as evidence for a significant contribution from events with photon fluctuation into Fock states with one or more gluons.

The data have been compared with the $\gamma^* p$ data of the EMC collaboration, with the $\gamma^* p$ CM energy (W) of the EMC inclusive DIS data similar to the $\gamma^* I\!P$ CM energy (M_X) of the H1 diffractive data. It is seen that additional transverse momentum is produced in diffractive scattering compared to the $\gamma^* p$ case. A striking contrast is observed in the seagull plot, indicating an approximate symmetry between the target and current hemispheres in diffractive DIS, as would be expected in the hard-gluon picture of the pomeron and in the photon dissociation picture, whereas radiation is significantly suppressed in the proton-remnant region in non-diffractive DIS.

The features of hadron production are well reproduced by a model featuring a factorisable pomeron flux in the proton if the partonic structure of the pomeron is dominated by hard gluons at the starting scale of $Q_0^2 = 3\,\mathrm{GeV}^2$ used in a DGLAP analysis of the diffractive structure function $F_2^{D(3)}$. In contrast, a model with a pomeron consisting, at low Q^2, primarily of quarks fails to describe the data in several respects. With respect to the $\gamma^* I\!P$ axis, the quark-based pomeron produces too little energy flow and particle production in the central region, but too much at large $|\eta|$ and $|x_F|$. In the p_T^{*2} and "seagull" distributions, this model produces too little transverse momentum. A model based on soft colour interactions (SCI) also gives an acceptable description of the data.

Acknowledgments

We are grateful to the HERA machine group, whose outstanding efforts have made and continue to make this experiment possible. We thank the engineers and technicians for their work in constructing and maintaining the H1 detector, our funding agencies for financial support, the DESY technical staff for their continual assistance, and the DESY directorate for the hospitality which they extend to the non-DESY members of the collaboration.

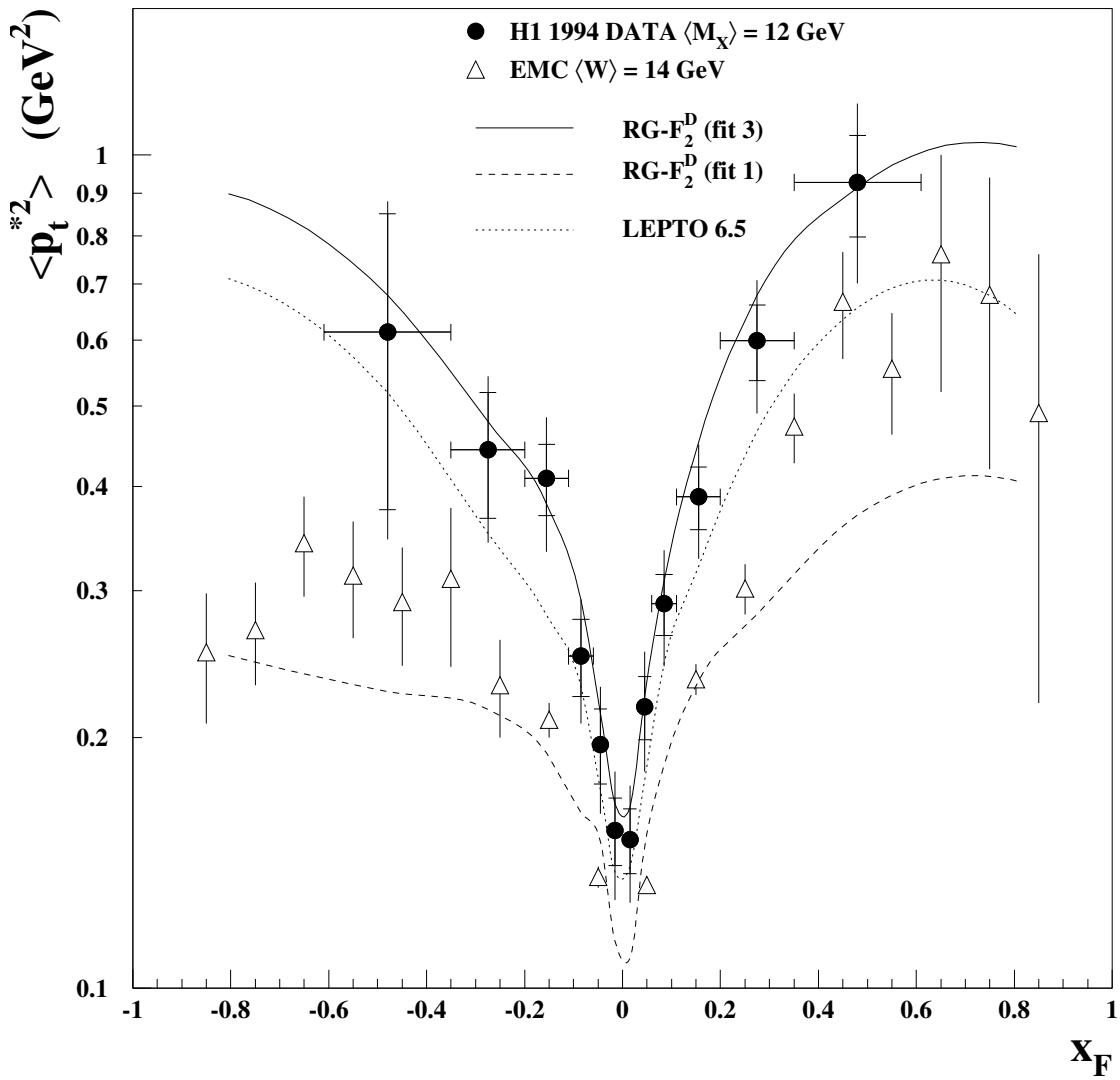

Figure 6: Seagull plot showing H1 $\gamma^* I\!P$ data in the $\gamma^* I\!P$ CM frame in the kinematic region $7.5 < Q^2 < 100\,\mathrm{GeV}^2$, $0.05 < y < 0.6$, $x_{I\!P} < 0.025$, $|t| < 1\,\mathrm{GeV}^2$, $M_Y < 1.6\,\mathrm{GeV}$ and $8 < M_X < 18\,\mathrm{GeV}$, together with EMC μp DIS data in the $\gamma^* p$ CM frame. Positive x_F corresponds to the direction of motion of the incoming photon. The points are plotted at the centre of the bin in the horizontal coordinate, and the horizontal bars indicate the width of the bin. Also shown are the predictions of the following Monte Carlo models for the H1 data: RAPGAP with the hard-gluon pomeron structure taken from fit 3 in [3] (RG–F_2^D (fit 3)); RAPGAP with the pomeron structure containing only quarks at the starting scale, taken from fit 1 in [3] (RG–F_2^D (fit 1)); and the soft colour interaction model as implemented in LEPTO 6.5.

References

[1] ZEUS Collaboration (M. Derrick et al.), Phys. Lett. B315 (1993) 481;
H1 Collaboration (T. Ahmed et al.), Nucl. Phys. B429 (1994) 477.

[2] H1 Collaboration (T. Ahmed et al.), Phys. Lett. B348 (1995) 681;
ZEUS Collaboration (M. Derrick et al.), Z. Phys. C68 (1995) 569.

[3] H1 Collaboration (C. Adloff et al.), Z. Phys. C76 (1997) 613.

[4] G. Altarelli and G. Parisi, Nucl. Phys. B126 (1977) 298;
Yu. L. Dokshitser, Sov. Phys. JETP 46 (1977) 641;
V. N. Gribov and L. N. Lipatov, Sov. J. Nucl. Phys. 15 (1972) 438, 675.

[5] ZEUS Collaboration (J. Breitweg et al.), DESY preprint 97–202, to be published in Phys. Lett. B.

[6] H1 Collaboration (C. Adloff et al.), Eur. Phys. J. C1 (1998) 495.

[7] P. Marage, Proceedings of the 5^{th} International Workshop on Deep Inelastic Scattering and QCD (DIS 97), Chicago, April 1997, World Scientific (1997).

[8] N. N. Nikolaev and B. G. Zakharov, Z. Phys. C53 (1992) 331;
A. Hebecker, Talk given at Madrid Workshop on Low-x Physics, Madrid, Spain, 18-21 June 1997, preprint hep–ph/9710475.

[9] J. D. Bjorken and J. Kogut, Phys. Rev. D8 (1973) 1341.

[10] A. Edin, G. Ingelman and J. Rathsman, Phys. Lett. B366 (1996) 371.

[11] G. Ingelman, A. Edin and J. Rathsman, Comp. Phys. Comm. 101 (1997) 108.

[12] H1 Collaboration (I. Abt et al.), Nucl. Instr. and Meth. A368 (1997) 310;
H1 Collaboration (I. Abt et al.), Nucl. Instr. and Meth. A368 (1997) 386.

[13] H1 Collaboration (S. Aid et al.), Nucl. Phys. B470 (1996) 3.

[14] A. Mehta, PhD thesis, University of Manchester 1994 (unpublished).

[15] H1 Collaboration (C. Adloff et al.), Z. Phys. C74 (1997) 221.

[16] C. M. Cormack, PhD thesis, University of Liverpool 1997 (unpublished).

[17] H. Jung, Comp. Phys. Comm. 86 (1995) 147;
H. Jung, *RAPGAP 2.02 Program Manual*, 1996 (unpublished).

[18] M. Bengtsson and T. Sjöstrand, Z. Phys. C37 (1988) 465;
M. Bengtsson, G. Ingelman and T. Sjöstrand, Proceedings of the HERA Workshop 1987, ed. R. D. Peccei, DESY, Hamburg, 1988.

[19] T. Sjöstrand, Comp. Phys. Comm. 82 (1994) 74.

[20] L. Lönnblad, Comp. Phys. Comm. 71 (1992) 15.

[21] A. Kwiatkowski, H. Spiesberger and H.-J. Möhring, Comp. Phys. Comm. 69 (1992) 155.

[22] J. F. Owens, Phys. Rev. D30 (1984) 943.

[23] A. D. Martin, W. J. Stirling and R. G. Roberts, Phys. Rev. D50 (1994) 6734.

[24] EMC Collaboration (M. Arneodo et al.), Phys. Lett. B149 (1984) 415;
EMC Collaboration (M. Arneodo et al.), Z. Phys. C35 (1987) 417.

[25] Yu. L. Dokshitzer, 1995 European School of High-Energy Physics, ed. N. Ellis, M. Neubert, CERN 96–04 (1996) p59.

[26] OPAL Collaboration (K. Ackerstaff et al.), Eur. Phys. J. C1 (1998) 479.

[27] G. D. Lafferty and T. R. Wyatt, Nucl. Instr. and Meth. A355 (1995) 541.